

A robust transfer matrix formulation for the ultrasonic response of multilayered absorbing media

Daniel Lévesque and Luc Piché

Industrial Materials Institute, National Research Council Canada, 75 De Mortagne, Boucherville, Québec J4B 6Y4, Canada

(Received 3 December 1991; accepted for publication 23 March 1992)

An improved version of the transfer matrix approach is presented for ultrasonic wave interaction in multilayered media. Generalized expressions are obtained for reflection and transmission coefficients in either fluid or solid half-space and problems associated with numerical stability are solved efficiently. The formulation is applicable to longitudinal and shear input waves alike, at arbitrary incidence angles and for any sequence of solid or fluid layers. Also, allowance is made for viscoelastic behavior by means of relaxation functions in the Laplace transform domain. Finally, the response to arbitrary incident pulse shapes and beam profiles is described through application of two-dimensional numerical Laplace inversion.

PACS numbers: 43.20.Fn, 43.20.Gp, 43.35.Mr

INTRODUCTION

The complete description of acoustic propagation in a multilayered system is of great interest in a variety of applications such as nondestructive evaluation and acoustic design, and there is need for a flexible model that can describe the reflection and transmission of ultrasonic waves in these media. A systematic approach to this question was presented by Thomson¹ and Haskell² who suggested a matrix method that transfers stress/displacement through interfaces. Although this transfer matrix approach can be used in principle,³ numerical algorithms based on its direct implementation are found to become unstable with increasing frequency.

The problem was first noticed by Dunkin,⁴ in connection with surface wave excitation, who indicated that working with the matrix of subdeterminants leads to a more robust algorithm. Since then, other schemes have been described, all of them leading to formulations that do not really ensure numerical stability.⁵⁻⁷ More recently, Kundu and Mal⁸ identified a second precision problem that occurs when computing the amplitude of the transmitted signal. The authors suggested an alternative that requires the computation of additional matrices and is therefore quite demanding. Problems with actual implementation of the method were not thoroughly examined. Finally, in a very recent paper, Cervenka and Challande⁹ presented a modified transfer matrix formalism oriented so as to include fluid behavior; however the ability of the method to avoid numerical instabilities has not been clearly established, particularly in the presence of evanescent waves.

Schmidt and Jensen¹⁰ proposed a different approach whereby local equations for two layer sets are mapped into a global system that comprises all unknowns associated with boundary conditions. In this case, effectiveness depends on the stability of the Gaussian elimination technique used in the numerical computation. For n layers with one source-

receiver combination, the transfer matrix technique is an n -operation process that involves multiplication of matrices of fixed small dimensions, while the mapping technique is an n^2 or even an n^3 operation process, depending on sparseness of the global system. The advantage of the Thomson-Haskell approach becomes obvious for large n , provided an efficient and stable formulation for its numerical implementation is available.

Here we describe a formulation that can handle any sequence of layers with great efficiency and yet overcome problems associated with computational instability. We derive general expressions for the reflection and transmission coefficients that relate to solid/fluid half-spaces and longitudinal/shear waves at arbitrary angles of incidence. Furthermore, the present formalism incorporates the viscoelastic behavior of solid or fluid constituents by use of relaxation functions that may involve fractional derivatives. The response to arbitrary pulse shapes and beam profiles is obtained by numerical Laplace inversion. Finally, our algorithm is quite robust, which constitutes a definite improvement over previous schemes.

In Sec. I, the field solutions to wave equations are derived in the transformed domain and special cases of excitation are considered. We also discuss relaxation functions that account for viscoelastic behavior and the use of an interface layer to handle different types of boundary conditions. In Sec. II, the procedure associated with the transfer matrix approach is presented and a basic system of equations is obtained for the reflection and transmission coefficients. There follows a short discussion concerning conservation of energy and evaluation of stresses and displacements. In Sec. III, we examine different computational schemes with respect to numerical stability. This leads to the description of a novel approach that is particularly robust. In Sec. IV, we discuss the details for an efficient implementation of the approach

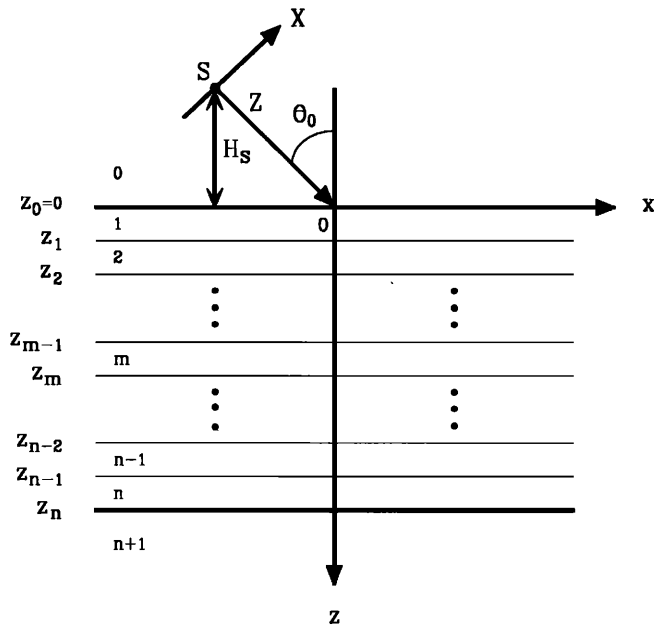


FIG. 1. Geometry of the multilayered system with half-spaces 0 and $n + 1$; S indicates the position of the acoustic source.

on a computer. Finally in Sec. V, several examples are given which illustrate the general features of the method.

I. FIELD EQUATIONS

We consider the laminated structure of Fig. 1 that comprises n parallel layers that are rigidly bonded at their interfaces. Each layer m of thickness $d_m = z_m - z_{m-1}$ and the half-spaces noted 0 and $n + 1$ on both sides of the system can be either a solid or a fluid with isotropic and homogeneous properties. The amplitude of the acoustic wave is considered small, so as to ensure linearity. The spatial variation of all quantities are limited to the x - z plane and internal sources are excluded from the analysis. Either a longitudinal wave (P wave) or a shear vertical wave (SV wave) is incident at the top surface $z = 0$, forming an angle θ_0 with the normal to the structure. These waves cannot be converted into shear horizontal waves (SH wave) and conversely, the propagation of SH waves therefore constitutes an independent problem, which is not considered here.

The system of equations that describes the displacements u and w along x and z , respectively, is written⁷

$$\left((\lambda + 2\mu) \frac{\partial^2}{\partial x^2} + \mu \frac{\partial^2}{\partial z^2} - \rho \frac{\partial^2}{\partial t^2} \right) u + (\lambda + \mu) \frac{\partial^2 w}{\partial x \partial z} = 0, \quad (1)$$

$$\left((\lambda + 2\mu) \frac{\partial^2}{\partial z^2} + \mu \frac{\partial^2}{\partial x^2} - \rho \frac{\partial^2}{\partial t^2} \right) w + (\lambda + \mu) \frac{\partial^2 u}{\partial x \partial z} = 0,$$

where λ and μ are the Lamé coefficients and ρ is the mass density at a given position x, z . The stresses, obtained from the constitutive relations, are

$$\begin{aligned} \sigma_{xx} &= (\lambda + 2\mu) \frac{\partial u}{\partial x} + \lambda \frac{\partial w}{\partial z}, \\ \sigma_{zz} &= (\lambda + 2\mu) \frac{\partial w}{\partial z} + \lambda \frac{\partial u}{\partial x}, \\ \sigma_{xz} &= \mu \left(\frac{\partial u}{\partial z} + \frac{\partial w}{\partial x} \right). \end{aligned} \quad (2)$$

The appropriate boundary conditions for rigidly bonded interfaces between layers m and $m + 1$ at $z = z_m$ are given by

$$\begin{aligned} u_m(z_m) &= u_{m+1}(z_m), \quad w_m(z_m) = w_{m+1}(z_m), \\ \sigma_{zz}^m(z_m) &= \sigma_{zz}^{m+1}(z_m), \quad \sigma_{xz}^m(z_m) = \sigma_{xz}^{m+1}(z_m). \end{aligned} \quad (3)$$

With the usual scheme for the decomposition of the displacement field⁴ in terms of the dilatational and shear potentials ϕ and ψ ,

$$u_m = \frac{\partial \phi_m}{\partial x} - \frac{\partial \psi_m}{\partial z}, \quad w_m = \frac{\partial \phi_m}{\partial z} + \frac{\partial \psi_m}{\partial x}, \quad (4)$$

one obtains equations that are coupled through boundary conditions only

$$\left(\frac{\partial^2}{\partial x^2} + \frac{\partial^2}{\partial z^2} \right) \phi_m = \frac{1}{c_{pm}^2} \frac{\partial^2}{\partial t^2} \phi_m, \quad (5)$$

$$\left(\frac{\partial^2}{\partial x^2} + \frac{\partial^2}{\partial z^2} \right) \psi_m = \frac{1}{c_{sm}^2} \frac{\partial^2}{\partial t^2} \psi_m,$$

where $c_{pm}^2 = (\lambda + 2\mu)/\rho$ and $c_{sm}^2 = \mu/\rho$ are the phase velocities for longitudinal and shear waves, respectively.

In the following, we shall make extensive use of Laplace-Laplace transforms relating the field functions $f(x, z, t)$ and $f(\xi, z, s)$ through

$$\begin{aligned} \bar{f}(\xi, z, s) &= \mathcal{L}_x \mathcal{L}_t \{ f(x, z, t) \}, \\ f(x, z, t) &= \mathcal{L}_t^{-1} \mathcal{L}_x^{-1} \{ \bar{f}(\xi, z, s) \}, \end{aligned} \quad (6a)$$

with the definitions

$$\begin{aligned} \mathcal{L}_x \mathcal{L}_t \{ f(x, z, t) \} &= \int_{-\infty}^{\infty} \int_0^{\infty} f(x, z, t) e^{-(st - \xi x)} dt dx, \quad (6b) \\ \mathcal{L}_t^{-1} \mathcal{L}_x^{-1} \{ \bar{f}(\xi, z, s) \} &= \frac{-1}{4\pi^2} \int_{\alpha - i\infty}^{\alpha + i\infty} \int_{\gamma - i\infty}^{\gamma + i\infty} \bar{f}(\xi, z, s) e^{(st - \xi x)} d\xi ds, \quad (6c) \end{aligned}$$

and where s and ξ are complex parameters for the variables t and x , respectively. The constants α and γ in Eq. (6c) denote the abscissa in the complex plane located to the right of any singularity associated with $\bar{f}(\xi, z, s)$. This choice calls for certain remarks. The Laplace transform \mathcal{L}_t is better adapted than the Fourier transform \mathcal{F} for the description of transient phenomena and viscoelastic behavior.^{11,12} Accordingly, the two-sided Laplace transform¹¹ \mathcal{L}_x constitutes the correct and most appropriate choice for the space variable x , as it allows both parameters s and ξ to be in the complex plane. This is also in line with recent theories related to superposition of inhomogeneous or evanescent plane waves.¹³ Furthermore, the transformation given by Eq. (6c) elimi-

nates the aliasing problem associated with discrete Fourier inversion. Finally, real physical situations satisfy the mathematical conditions for the existence of a Laplace–Laplace transformation on $f(x,z,t)$.

In the transformed domain, solutions to Eqs. (5) within each layer m can be written as

$$\begin{aligned}\bar{\phi}_m &= A_m e^{-h_m(z-z_{m-1})} + B_m e^{h_m(z-z_{m-1})} \\ &= \bar{\phi}_m^+ + \bar{\phi}_m^-, \\ \bar{\psi}_m &= C_m e^{-k_m(z-z_{m-1})} + D_m e^{k_m(z-z_{m-1})} \\ &= \bar{\psi}_m^+ + \bar{\psi}_m^-, \end{aligned} \quad (7)$$

with

$$\begin{aligned}h_m^2 &= s^2/c_{pm}^2 - \xi^2, \quad \text{Im}\{h_m\} \geq 0, \\ k_m^2 &= s^2/c_{sm}^2 - \xi^2, \quad \text{Im}\{k_m\} \geq 0, \end{aligned} \quad (8)$$

and where the superscripts $+$ and $-$ refer to waves propagating, respectively, in the positive and negative directions. A recurrence relation that permits solving for the unknown coefficients in Eqs. (7) will be given in Sec. II, in the frame of the so-called transfer matrix approach. First, we proceed with a discussion on the application of the above formalism to practical situations.

As usual for linear systems, the response (output signal) can be related to the excitation (input signal) through a series of convolutions.¹² In the transformed domain, this is expressed through

$$\bar{f}(\xi, z, s) = \bar{H}(\xi, z, s) \bar{E}_1(\xi, s) \bar{E}_2(s), \quad (9)$$

where \bar{H} is the transfer function of the multilayered system obtained by solving Eqs. (7), \bar{E}_1 is the two-sided Laplace transform \mathcal{L}_x of the input beam profile at the surface $z = 0$, and \bar{E}_2 is the Laplace transform \mathcal{L}_t of the source history.

An interesting case is that of beams with Gaussian profiles in order to minimize diffraction effects. Although we restrict our analysis to incident P waves, similar expressions for SV waves can be obtained by replacing c_{p0} with c_{s0} . In the case of a beam having a width $2b$ and incidence angle θ_0 , the transformed function $\bar{E}_1(\xi, s)$ is written

$$\bar{E}_1(\xi, s) = \int_{-\infty}^{\infty} B_0(x, s) e^{\xi x} dx, \quad (10)$$

where $B_0(x, s)$ is the profile at the surface $z = 0$ which is described by^{3,14}

$$B_0(x, s) = e^{-(x \cos \theta_0/b)^2} e^{-\xi_0 x}. \quad (11)$$

The quantity $b/\cos \theta_0$ is the beam width at the intercept with surface $z = 0$ and $\xi_0 = s \sin \theta_0/c_{p0}$. Here, we note that Eq. (11) is a function of two parameters, b and θ_0 , which do not involve position of the source, and implies that the incident beam is focused at the surface $z = 0$.

A good approximation to a Gaussian beam is provided by a spherical source with complex space coordinates.^{14,15} The analysis presented in Refs. 14 and 15 pertained to Fourier domain ($i\omega$) and here, we extend these results to the

Laplace domain (s). As shown in Fig. 1, a transducer located at $S = (-H_s \tan \theta_0, -H_s)$, generates a bounded beam along Z , which may be described through

$$B(X, Z, s) = (B_n/D) e^{-sD/c_{p0}}, \quad (12)$$

$$D = \sqrt{X^2 + (Z + \beta)^2},$$

where B_n is a normalizing constant such that $B(0, 0, s) = 1$ at the source location S , D is the complex distance to the source, and β is a complex parameter characterizing beam spreading. In the limit of $X/|Z + \beta| \ll 1$, Eqs. (12) represent a Gaussian profile¹⁴ with a beam width $2b$ which itself depends on Z . At position S , the parameter β is related to the beam width through

$$\beta = sb^2/2c_{p0}. \quad (13)$$

The profile $B_0(x, s)$ is obtained by expressing the coordinates X and Z in terms of x and θ_0 at the surface $z = 0$ and evaluating the factor B_n . One finds

$$B_0(x, s) = (\beta/D) e^{-s/c_{p0}(D-\beta)} \quad (14a)$$

with values of X and Z in D given by

$$X = x \cos \theta_0, \quad (14b)$$

$$Z = H_s/\cos \theta_0 + x \sin \theta_0,$$

which involves three parameters b , θ_0 , and H_s .

Since our approach concerns two-dimensional problems only, we chose to consider cylindrical sources, in which case, Eq. (14a) is replaced by

$$B_0(x, s) = \sqrt{\beta/D} e^{-s/c_{p0}(D-\beta)}. \quad (15)$$

However, we verified that Eq. (14a) and Eq. (15) lead to results that are qualitatively identical, so that Eq. (14a) is a satisfactory approximation in many situations. By performing a numerical Laplace transformation one arrives at $\bar{E}_1(\xi, s)$ and complete Laplace–Laplace inversion leads to the full solution $f(x, z, t)$.

For a plane wave, one has $B_0(x, s) = e^{-\xi_0 x}$ and the transformed function is simply $\bar{E}_1(\xi, s) = \delta(\xi - \xi_0)$, δ being the Dirac delta function. After substitution in Eqs. (6), the response function is written

$$f(x, z, t) = \mathcal{L}_t^{-1}\{\bar{H}(\xi_0, z, s) \bar{E}_2(s) e^{-\xi_0 x}\} \quad (16)$$

so that the transfer function needs to be evaluated only at $\xi = \xi_0$ and the full solution is found after single Laplace inversion. For the case of a bounded beam with a temporal excitation at angular frequency ω , the parameter s is replaced by the value $i\omega$ and the time response is given by

$$\bar{f}(x, z, \omega) = \mathcal{L}_x^{-1}\{\bar{H}(\xi, z, i\omega) \bar{E}_1(\xi, i\omega)\}, \quad (17)$$

$$f(x, z, t) = \text{Re}\{\bar{f}(x, z, \omega) e^{i\omega t}\},$$

where $\text{Re}\{ \}$ means the “real part of.”

A second point concerns absorption of energy. Most often, this is accounted for by introducing complex moduli for the material properties. A more complete approach for viscoelastic materials relates the stress–strain fields through a

series of time derivatives.^{16,17} The major drawback here is that a large number of terms is required to describe the behavior over a wide range of frequency. To deal with this, it was suggested¹⁸ that fractional calculus could serve as a basis for modeling viscoelasticity. Indeed, the fractional derivative operator D^r can be written¹⁸ in a form that makes it an interesting starting point for the description of memory effects:

$$D^r[f(t)] = \frac{1}{\Gamma(1-r)} \frac{d}{dt} \int_0^t \frac{f(t-\tau)}{\tau^r} d\tau, \quad (18)$$

with $0 < r \leq 1$ and Γ being the gamma function. While considered purely empirical, the model has long proven to be a powerful means for describing experimental results. This has stimulated recent theoretical efforts¹⁹ seeking some physical implications.

It is found that constitutive relations involving fractional derivative operators are compatible with the elastic-viscoelastic correspondence principle.¹⁶ Hence, in the Laplace transform domain, one simply replaces λ and μ in Eqs. (7) by relaxation functions

$$\bar{\lambda}(s) = \frac{\lambda_0 + \sum_{j=1}^J \lambda_j s^{\hat{\alpha}_j}}{1 + \sum_{k=1}^K a_k s^{\hat{\beta}_k}}, \quad \bar{\mu}(s) = \frac{\mu_0 + \sum_{l=1}^L \mu_l s^{\alpha_l}}{1 + \sum_{p=1}^P b_p s^{\beta_p}}. \quad (19)$$

For a system with one degree of freedom only, Eq. (19) becomes

$$\bar{\lambda} = \frac{\lambda_0 + \lambda_1 s^r}{1 + a s^r}, \quad \bar{\mu} = \frac{\mu_0 + \mu_1 s^r}{1 + a s^r}, \quad (20)$$

which imply fractional derivatives in the time domain. Substituting the following parameters:

$$\begin{aligned} \lambda_0 &= \bar{\lambda}(0), \quad \lambda_\infty = \bar{\lambda}(i\infty) = \lambda_1/a, \\ \mu_0 &= \bar{\mu}(0), \quad \mu_\infty = \bar{\mu}(i\infty) = \mu_1/a, \\ \tau &= a, \end{aligned} \quad (21)$$

into Eqs. (20), one arrives at

$$\frac{\bar{\lambda}(s) - \lambda_0}{\lambda_\infty - \lambda_0} = \frac{(s\tau)^r}{1 + (s\tau)^r}, \quad \frac{\bar{\mu}(s) - \mu_0}{\mu_\infty - \mu_0} = \frac{(s\tau)^r}{1 + (s\tau)^r}, \quad (22)$$

where τ is an effective relaxation time and r is the fractional order. These expressions are identical to the empirical relaxation functions proposed by Cole-Cole in 1941 for the dielectric problem.²⁰ For a viscoelastic fluid one simply has¹⁶

$$\mu_0 = \bar{\mu}(0) \rightarrow 0 \quad (23)$$

and for the limiting case of classical fluids, with $r = 1$, $a = 0$ in Eqs. (20), the relaxation functions become

$$\bar{\lambda} = K_0 + (\zeta - 2\eta/3)s, \quad \bar{\mu} = \eta s, \quad (24)$$

where K_0 is the bulk modulus, and η and ζ are the first and second coefficients of viscosity.

Another significant point concerns boundary conditions. In the above, we assumed rigid bonding between all components. Usually one makes this assumption for perfectly matched interfaces between solids. In the opposite case, for the interface between a solid and a classical nonviscous

fluid, one usually considers slip boundary conditions corresponding to vanishing shear stress and allowing discontinuity of tangential displacement. While they may lead to useful results in many cases, these descriptions are approximate. Sharp discontinuities are forbidden by thermodynamics so that an interface is really an interfacial region or, in the language of hydrodynamics, a boundary layer. Very generally, one may model an interface by introducing a very thin layer,²¹ rigidly bonded to its neighbors, with effective viscoelastic properties that can be adjusted to represent boundary conditions where bonding ranges from rigid (welded) to slip (smooth).

II. TRANSFER MATRIX FORMALISM

Now, we describe the basis for the transfer matrix approach. For each layer m , two vectors are defined, namely, the potential vector p_m and the field vector q_m (Ref. 4),

$$\{p_m(z)\} = \langle \bar{\phi}_m^+ \quad \bar{\psi}_m^+ \quad \bar{\phi}_m^- \quad \bar{\psi}_m^- \rangle^T, \quad (25)$$

$$\{q_m(z)\} = \langle \bar{u}_m \quad \bar{w}_m \quad \bar{\sigma}_{zz}^m \quad \bar{\sigma}_{xz}^m \rangle^T$$

where $z_{m-1} \leq z \leq z_m$, the superscript T refers to the transpose operator, while $\{ \}$ and $\langle \rangle$ stand for column and row vector, respectively. At any position z in the layer, matrix relations exist between these vectors, as given by

$$\{q_m(z)\} = [T_m] \{p_m(z)\}, \quad (26)$$

$$\{p_m(z)\} = [T_m]^{-1} \{q_m(z)\},$$

with

$$[T_m] = \begin{bmatrix} -\xi & k & -\xi & -k \\ -h & -\xi & h & -\xi \\ \gamma & 2\mu\xi k & \gamma & -2\mu\xi k \\ 2\mu\xi h & -\gamma & -2\mu\xi h & -\gamma \end{bmatrix}_m, \quad (27a)$$

$$[T_m]^{-1} = \frac{1}{2\rho_m s^2} \times \begin{bmatrix} -2\mu\xi & -\gamma/h & 1 & \xi/h \\ \gamma/k & -2\mu\xi & \xi/k & -1 \\ -2\mu\xi & \gamma/h & 1 & -\xi/h \\ -\gamma/k & -2\mu\xi & -\xi/k & -1 \end{bmatrix}_m, \quad (27b)$$

where $[\]_m$ indicates that the matrix is evaluated with the properties of layer m and $\gamma_m = \rho_m s^2 - 2\mu_m \xi^2$. Also, one notes the following relation between potential vectors on both faces of the layer m :

$$\{p_m(z_m)\} = [E_m] \{p_m(z_{m-1})\}, \quad (28)$$

with

$$[E_m] = \begin{bmatrix} \exp(-hd) & 0 & 0 & 0 \\ 0 & \exp(-kd) & 0 & 0 \\ 0 & 0 & \exp(hd) & 0 \\ 0 & 0 & 0 & \exp(kd) \end{bmatrix}_m \quad (29)$$

and $d_m = z_m - z_{m-1}$.

Hence, for boundary conditions corresponding to rigid bonding at the interface $z = z_m$ between layers m and $m + 1$, there is the matrix relation

$$\{q_{m+1}(z_m)\} = \{q_m(z_m)\}, \quad (30)$$

which can be rewritten as

$$\begin{aligned} \{q_{m+1}(z_m)\} &= [T_m] \{p_m(z_m)\} \\ &= [T_m] [E_m] \{p_m(z_{m-1})\} \\ &= [T_m] [E_m] [T_m]^{-1} \{q_m(z_{m-1})\} \\ &= [A_m] \{q_m(z_{m-1})\}. \end{aligned} \quad (31)$$

The last expression is a recurrence formula that relates the fields on top of layer m to those on top of layer $m + 1$. The so-called transfer matrix $[A_m]$ serves to propagate the stress-displacement response downward through a layer and then across the next interface. Starting with an excitation at the top surface $z = 0$ and noting that $q_1(0) = q_0(0)$, successive application of Eq. (31) through media 0 to $n + 1$ yields

$$\{q_{n+1}(z_n)\} = [J] \{q_0(0)\},$$

where

$$[J] = [A_n] [A_{n-1}] \cdots [A_2] [A_1]. \quad (32)$$

There are generally two reflected components on the top and two transmitted components on the bottom. This suggests the following definitions for the reflection (r) and transmission (t) coefficients in terms of the potentials,²²

$$\begin{aligned} r_p &= \bar{\phi}_0^- / \bar{\phi}_0^+, & r_s &= \bar{\psi}_0^- / \bar{\phi}_0^+, \\ t_p &= \bar{\phi}_{n+1}^+ / \bar{\phi}_0^+, & t_s &= \bar{\psi}_{n+1}^+ / \bar{\phi}_0^+, \end{aligned} \quad (33)$$

where subscripts p and s stand for the longitudinal and shear components, respectively. For an incident P wave, one obtains

$$\begin{Bmatrix} t_p \\ t_s \\ 0 \\ 0 \end{Bmatrix} = [T_{n+1}]^{-1} [J] [T_0] \begin{Bmatrix} 1 \\ 0 \\ r_p \\ r_s \end{Bmatrix} = [G] \begin{Bmatrix} 1 \\ 0 \\ r_p \\ r_s \end{Bmatrix}, \quad (34)$$

which constitutes a system of four equations with four unknowns. For an incident SV wave, the system of equations is

$$\begin{Bmatrix} t_p \\ t_s \\ 0 \\ 0 \end{Bmatrix} = [T_{n+1}]^{-1} [J] [T_0] \begin{Bmatrix} 1 \\ 0 \\ r_p \\ r_s \end{Bmatrix} = [G] \begin{Bmatrix} 0 \\ 1 \\ r_p \\ r_s \end{Bmatrix}. \quad (35)$$

Once t_p , t_s , r_p , and r_s have been evaluated, the stress-displacement transfer function $\bar{H}(\xi, z, s)$ in Eq. (9) is obtained through application of Eqs. (26)–(29) to media 0 and $n + 1$. Formally, for an incident P wave, one finds for media 0 at $z = 0$

$$\begin{aligned} \bar{u} &= -\xi(1 + r_p) - k_0 r_s, \\ \bar{w} &= -h_0(1 - r_p) - \xi r_s, \\ \bar{\sigma}_{zz} &= \gamma_0(1 + r_p) - 2\mu_0 \xi k_0 r_s, \\ \bar{\tau}_{xz} &= 2\mu_0 \xi h_0(1 - r_p) - \gamma_0 r_s, \end{aligned} \quad (36)$$

while for media $n + 1$ at $z = z_n$, the result is

$$\begin{aligned} \bar{u} &= -\xi t_p - k_{n+1} t_s, \\ \bar{w} &= h_{n+1} t_p - \xi t_s, \\ \bar{\sigma}_{zz} &= \gamma_{n+1} t_p - 2\mu_{n+1} \xi k_{n+1} t_s, \\ \bar{\sigma}_{xz} &= -2\mu_{n+1} \xi h_{n+1} t_p - \gamma_{n+1} t_s. \end{aligned} \quad (37)$$

The complete stress-displacement field equations $f(x, z, t)$ are obtained from Eqs. (6)–(9). To describe viscoelastic behavior, the coefficients λ and μ are replaced by appropriate relaxation functions, Eqs. (22). However, when either of these media is a fluid, one should use the coefficients in Eqs. (24) and for small viscosities η and ζ , Eqs. (36) and (37) reduce to

$$\begin{aligned} \bar{u} &\rightarrow u_0(\text{constant}), \\ \bar{w} &\rightarrow -h_0(1 - r_p), \\ \bar{\sigma}_{zz} &\rightarrow \rho_0 s^2(1 + r_p) = -P, \\ \bar{\sigma}_{xz} &\rightarrow 0, \end{aligned} \quad (38)$$

for media 0, and

$$\begin{aligned} \bar{u} &\rightarrow u_{n+1}(\text{constant}), \\ \bar{w} &\rightarrow h_{n+1} t_p, \\ \bar{\sigma}_{zz} &\rightarrow \rho_{n+1} s^2 t_p = -P, \\ \bar{\sigma}_{xz} &\rightarrow 0, \end{aligned} \quad (39)$$

for media $n + 1$, where P is the acoustic pressure. Hence, Eqs. (36) and (37) constitute a generalization of previous results.²² For the case of SV waves, one arrives at equations similar to Eqs. (36) and (37).

In practice, one is often interested in the reflection and transmission coefficients associated with propagation of energy. The time average of the power flow per unit area through the surface normal to z is given by^{3,13}

$$W = -\frac{1}{2} \text{Re} \left\{ \langle \sigma_{zz} \quad \sigma_{xz} \rangle \begin{Bmatrix} i\omega w \\ i\omega u \end{Bmatrix}^* \right\}, \quad (40)$$

where $*$ indicates the complex conjugate. For an incident P wave, the following relation must hold:

$$W_{ip} = W_{rp} + W_{rs} + W_{tp} + W_{ts} + W_{\text{abs}},$$

where i, r, t refer to incident, reflected, and transmitted energy components and W_{abs} represents absorption losses. In absence of absorption, one finds

$$|r_p|^2 + |r_s|^2 q_{s0}/q_{p0} + |t_p|^2 q_{pn}/q_{p0} + |t_s|^2 q_{sn}/q_{p0} = 1, \quad (41)$$

where

$$q_{p0} = \text{Re}\{i\rho_0 h_0^* \}, \quad q_{s0} = \text{Re}\{i\rho_0 k_0^* \}, \quad (42)$$

$$q_{pn} = \text{Re}\{i\rho_{n+1} h_{n+1}^* \}, \quad q_{sn} = \text{Re}\{i\rho_{n+1} k_{n+1}^* \}.$$

This yields the following energy coefficients:

$$R_p = |r_p|^2, \quad R_s = |r_s|^2 q_{s0}/q_{p0}, \quad (43)$$

$$T_p = |t_p|^2 q_{pn}/q_{p0}, \quad T_s = |t_s|^2 q_{sn}/q_{p0},$$

and the sum of these coefficients is less than one for a multi-layered absorbing media. Similarly, for an incident *SV*-wave, one arrives at

$$R_p = |r_p|^2 q_{p0}/q_{s0}, \quad R_s = |r_s|^2, \quad (44)$$

$$T_p = |t_p|^2 q_{pn}/q_{s0}, \quad T_s = |t_s|^2 q_{sn}/q_{s0}.$$

III. THE PRECISION PROBLEM

The question of numerical stability arises when evaluating the reflection and transmission coefficients, Eqs. (34) and (35). Here, we study the stability of different computational schemes in the case of an incident *P* wave. We then derive a stable formulation applicable to both incident *P* waves and *SV* waves.

The most obvious solution to Eqs. (34) is written in the form

$$r_p = -G_{14}^{34}/G_{34}^{34}, \quad r_s = G_{13}^{34}/G_{34}^{34}, \quad (45)$$

$$t_p = G_{11} + G_{13}r_p + G_{14}r_s, \quad t_s = G_{21} + G_{23}r_p + G_{24}r_s,$$

with

$$G_{kl}^{ij} = G_{ik}G_{jl} - G_{il}G_{jk}. \quad (46)$$

It has been shown by Dunkin⁴ that elements of $[J]$ contain terms such as

$$(a_1 - a_2) \exp(2h_m d_m), \quad (47)$$

where a_1 and a_2 are equal. When using numerical techniques to evaluate $[J]$, the exponential term may cause large amplification of roundoff errors, especially in the presence of evanescent waves for large values of fd_m . In ultrasonic applications, fd_m can be of the order of 10^2 MHz·mm and the calculation procedure may well happen to fail in a range that is of the most interest.⁶

To assess the effect of roundoff errors on the calculation of ultrasonic reflection and transmission coefficients, we consider as a simple example the system "water-steel-water." Material properties are given in Table I where α_p , α_s refer to attenuation around 20 MHz, respectively, for longitudinal and shear components. We investigate numerical stability in calculating the reflection and transmission coefficients

TABLE I. Physical properties of materials.

Materials	ρ (kg/m ³)	λ (GPa)	μ (GPa)	α_p (m ⁻¹)	α_s (m ⁻¹)
Water	1000	2.19	0	0.5	10 ⁶
Stainless steel	7930	113	75	35	100
Copper	8900	106	46	15	35
Nickel	8800	125	77	15	25
Silver	10500	82	27	20	50

of energy [Eqs. (43)] as a function of the incidence angle θ_0 for a fixed frequency f and different steel layer thicknesses d . We used a PC 486 compatible computer and the code was written in FORTRAN with Double Complex (16 bytes) arithmetic; however similar results were obtained with a MicroVax 3500 machine.

In Fig. 2, we show results for reflection and transmission coefficients of energy corresponding to Eqs. (45). Starting from the bottom of the figures, the different curves relate to increasing values of thickness, $d = 0.2, 0.5, 1, 1.5,$ and 2 mm, at constant frequency $f = 20$ MHz. As expected for a fluid, R_s is found to be zero everywhere and therefore, we omitted the figure associated with this coefficient. At small thickness values $d < 0.2$ mm, Rayleigh behavior is obvious in R_p and T_s for $\theta_0 > \theta_{cs}$, $\theta_{cs} \sim 28.7^\circ$ being the shear critical angle. Here, we point out that Rayleigh waves are made to occur simply by accounting for attenuation and that there is no need for an *ad hoc* arbitrary⁶ real component to ξ_0 . For $d \geq 0.5$ mm, R_p and T_s exhibit manifestations for Lamb modes at θ values lying between the longitudinal and shear critical angles $\theta_{cp} \approx 14.9^\circ$ and $\theta_{cs} \approx 28.7^\circ$. When $d \geq 1$ mm, the computational scheme leads to instabilities for R_p , T_p , and T_s , precluding any kind of analysis for wave behavior.

The question of stability may be given a more global representation by illustrating the results in the form of a phase diagram. As a criterion, cases where the sum of the energy coefficients [Eqs. (43)] exceeds unity by more than 1% were classified unstable. In Fig. 3, we plot the minimum value of $\sin \theta_0$ for the onset of instability as a function of fd , and curves 1, 2, and 3 represent the boundary between stable (regions on the left) and unstable (regions on the right) solutions. For the scheme corresponding to Eqs. (45) and illustrated in Fig. 2, the phase boundary is given by curve 1 in Fig. 3. The diagram shows that numerical stability is ensured provided $fd < 9$ MHz·mm, or $\sin \theta_0 < 0.3$, coinciding with the critical angle where longitudinal waves become evanescent; otherwise the system may easily become unstable.

In order to improve stability, Dunkin⁴ introduced the so-called delta matrix operator $[A]^\Delta$ made up of all 2×2 subdeterminants of $[A]$. Formally in this case, one has

$$A_{ij}^\Delta = A_{rs}^{pq}, \quad (48)$$

where the paired indices pq or $rs = 12, 13, 14, 23, 24,$ and 34 , corresponding to i or $j = 1, 2, 3, 4, 5,$ and 6 , respectively. The delta operator has the property

$$([A][B])^\Delta = [A]^\Delta[B]^\Delta, \quad (49)$$

which, when applied to the matrix $[G]$, leads to

$$[G]^\Delta = [T_{n+1}]^{-\Delta} [A_n]^\Delta \cdots [A_1]^\Delta [T_0]^\Delta, \quad (50a)$$

where

$$[A_m]^\Delta = [T_m]^\Delta [E_m]^\Delta [T_m]^{-\Delta} \quad (50b)$$

must be obtained analytically. Since the inversion and delta operators do not commute, the notation $[B]^{-\Delta}$ may be ambiguous: here we define $[B]^{-\Delta} \equiv [[B]^{-1}]^\Delta$. With this, the reflection and transmission coefficients are written

$$r_p = -G_{63}^\Delta/G_{66}^\Delta, \quad r_s = G_{62}^\Delta/G_{66}^\Delta, \quad (51a)$$

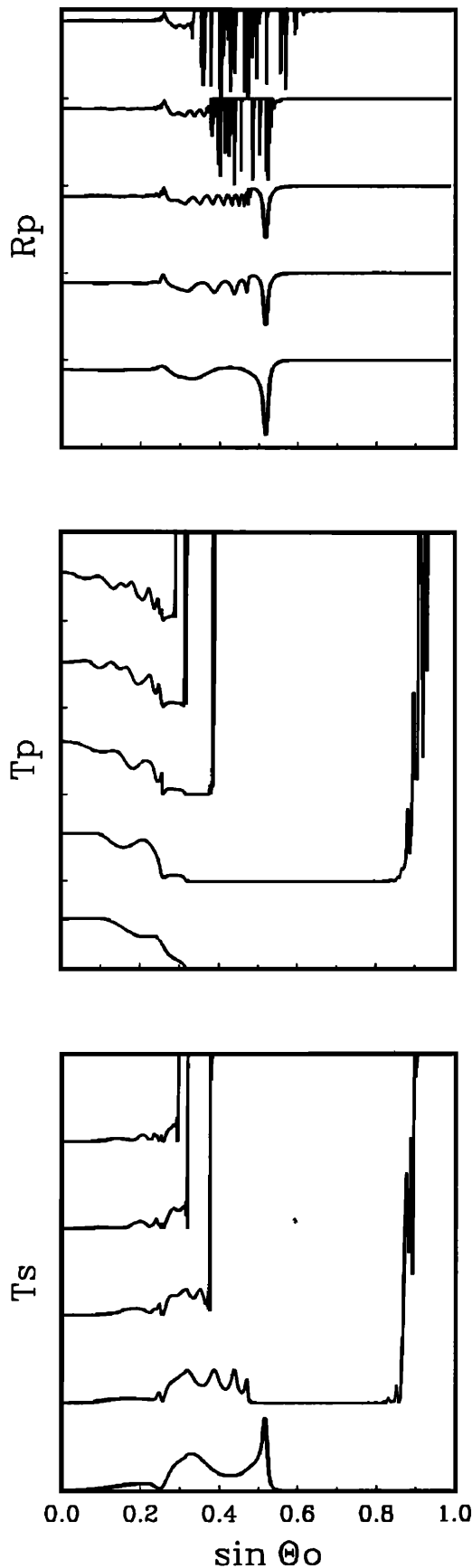


FIG. 2. Angular spectrum for R_p (range 0–1), T_p (range 0–0.2) and T_s (range 0–0.5) obtained at 20 MHz using Eqs. (45) for the system “water–steel–copper.” Starting from bottom, d (steel) = 0.2, 0.5, 1, 1.5, and 2 mm.

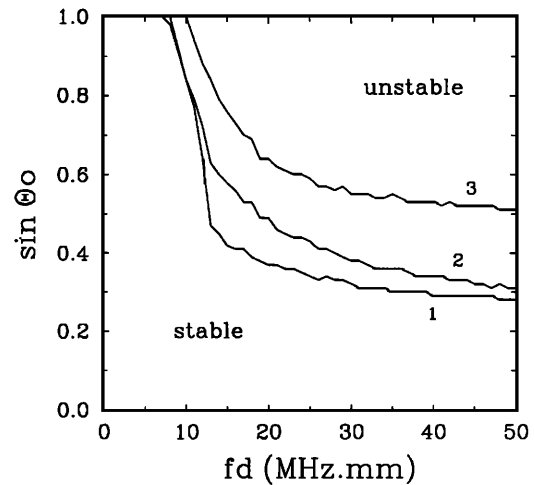


FIG. 3. Phase diagram illustrating numerical stability in the plane fd - $\sin \theta_0$ for the system “water–steel–copper.” Curves 1, 2, and 3 refer to use of Eqs. (45), (51), and (52), respectively.

$$t_p = G_{11} + G_{13}r_p + G_{14}r_s, \quad t_s = G_{21} + G_{23}r_p + G_{24}r_s, \quad (51b)$$

where $[G]$ and $[G]^\Delta$ are computed separately. The matrices $[T_{n+1}]^{-\Delta}$ and $[T_0]^\Delta$ can be evaluated numerically from $[T_m]$ since exponential terms are not involved. Curve 2 of Fig. 3 shows that the scheme corresponding to Eqs. (51) provides only minor improvement over Eqs. (45). In fact, the approach of Dunkin⁴ is very effective in suppressing instabilities of the reflected signal, but much less so for the transmitted signal, where instabilities set in that govern the boundary line 2.

Even when r_p and r_s are stable, expressions (51b) for the transmission coefficients involve combinations of elements from $[G]$, which lead to instabilities. Since there appear to be no instabilities associated with $[G]^\Delta$, one should try expressing the coefficients as a linear combination of this matrix. By adding and subtracting terms in Eqs. (51b), one arrives at

$$\begin{aligned} r_p &= -G_{63}^\Delta/G_{66}^\Delta, \quad r_s = G_{62}^\Delta/G_{66}^\Delta, \\ t_p &= (G_{33}^\Delta G_{22}^\Delta - G_{23}^\Delta G_{32}^\Delta)/(G_{11}^\Delta G_{66}^\Delta), \\ t_s &= (G_{53}^\Delta G_{42}^\Delta - G_{43}^\Delta G_{52}^\Delta)/(G_{21}^\Delta G_{66}^\Delta). \end{aligned} \quad (52)$$

The corresponding result is shown by curve 3 in Fig. 3. Numerical instabilities persist in the region where the angle of incidence exceeds the shear critical angle and both transmission coefficients are zero. Thus, in principle, an algorithm based on Eqs. (52) would appear to be satisfactory, provided it is used with caution.

Nonetheless, it would be preferable to eliminate instabilities completely. Starting from an idea by Kundu and Mal,⁸ one could consider working with matrices $[G]^{-1}$ and $[G]^{-\Delta}$ in addition to $[G]$ and $[G]^\Delta$. While at first sight, this approach is not very attractive, in fact it constitutes the basis for our more global and robust formulation.

Let us express the previous system of Eqs. (34) for an incident P wave in the form

$$\begin{Bmatrix} 1 \\ 0 \\ r_p \\ r_s \end{Bmatrix} = [G]^{-1} \begin{Bmatrix} t_p \\ t_s \\ 0 \\ 0 \end{Bmatrix} = [H] \begin{Bmatrix} t_p \\ t_s \\ 0 \\ 0 \end{Bmatrix}. \quad (53)$$

Making use of the definition $[H]^\Delta = [G]^{-\Delta}$, we derive the following expressions for the transmission coefficients:

$$t_p = H_{22}^\Delta / H_{11}^\Delta, \quad t_s = -H_{21}^\Delta / H_{11}^\Delta \quad (54a)$$

and the reflection coefficients

$$r_p = H_{31}^\Delta t_p + H_{32}^\Delta t_s, \quad r_s = H_{41}^\Delta t_p + H_{42}^\Delta t_s. \quad (54b)$$

Substitution of Eqs. (54a) in Eqs. (54b) yields the interesting result

$$r_p = -H_{41}^\Delta / H_{11}^\Delta, \quad r_s = -H_{51}^\Delta / H_{11}^\Delta, \quad (55)$$

$$t_p = H_{22}^\Delta / H_{11}^\Delta, \quad t_s = -H_{21}^\Delta / H_{11}^\Delta,$$

which involves only discrete components of $[H]$ and $[H]^\Delta$, while matrices $[G]$ and $[G]^\Delta$ are no longer implicated.

Similarly for an incident *SV* wave, the system of equations (35) becomes

$$\begin{Bmatrix} 0 \\ 1 \\ r_p \\ r_s \end{Bmatrix} = [H] \begin{Bmatrix} t_p \\ t_s \\ 0 \\ 0 \end{Bmatrix} \quad (56)$$

and the four coefficients are given by

$$\begin{aligned} r_p &= H_{21}^\Delta / H_{11}^\Delta, & r_s &= H_{31}^\Delta / H_{11}^\Delta, \\ t_p &= -H_{12}^\Delta / H_{11}^\Delta, & t_s &= H_{11}^\Delta / H_{11}^\Delta. \end{aligned} \quad (57)$$

It is noteworthy that for either type of wave, only the first column of $[H]^\Delta$ is involved and computation of these matrices is not a difficult task. The matrix $[H]$ can be explicitly written as

$$\begin{aligned} [H] &= [G]^{-1} \\ &= [T_0]^{-1} [A_1]^{-1} \cdots [A_n]^{-1} [T_{n+1}] \\ &= [T_0]^{-1} [B_1] \cdots [B_n] [T_{n+1}]. \end{aligned} \quad (58)$$

The remaining problem lies in the calculation of $[B_m]$. Since $[A_m] = [T_m] [E_m] [T_m]^{-1}$, one simply has

$$[B_m] = [T_m] [E_m]^{-1} [T_m]^{-1} \quad (59)$$

and so, matrices $[B_m]$ and $[B_m]^\Delta$ are obtained from $[A_m]$ and $[A_m]^\Delta$ by replacing d_m by $-d_m$ into $[E_m]$.

Figure 4 shows that the numerical results for Eqs. (55) and (57) are completely stable. We have investigated a number of different examples corresponding to values fd up to 200 MHz·mm with equal success, indicating that our scheme is indeed quite robust.

IV. COMPUTATIONAL PROCEDURE

In summary, one needs to compute the following matrices:

$$[H] = [T_0]^{-1} [B_1] \cdots [B_n] [T_{n+1}], \quad (60)$$

$$[H]^\Delta = [T_0]^{-\Delta} [D_1] \cdots [D_n] [T_{n+1}]^\Delta,$$

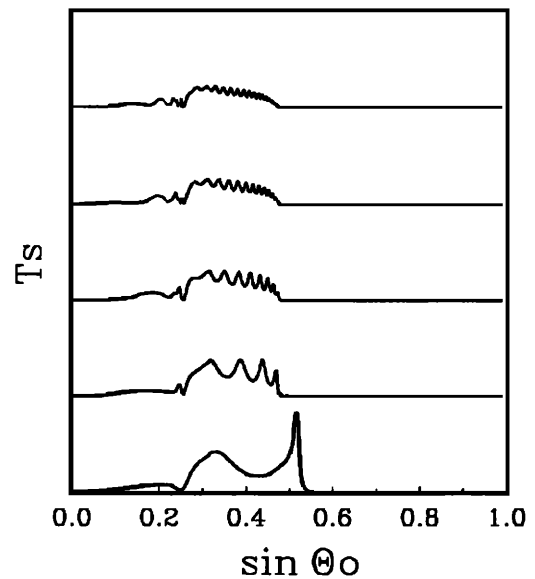
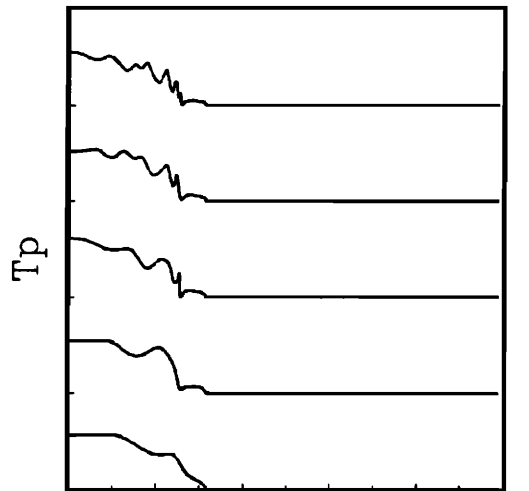
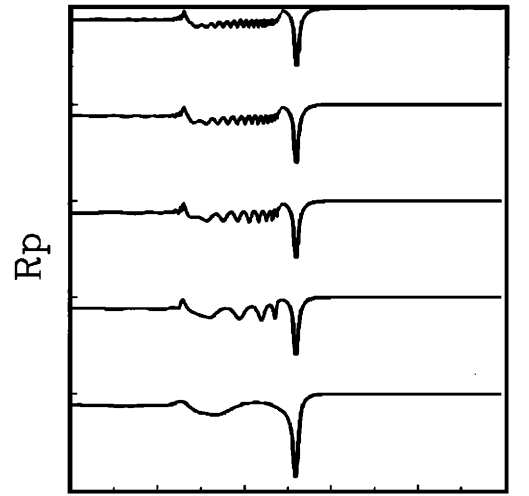


FIG. 4. Same as in Fig. 2 but with results from the stable set of Eqs. (55).

where $[B_m]$ and $[D_m] \equiv [B_m]^A$ are given in the Appendix. The reflection and transmission coefficients are obtained from Eqs. (55) or (57), depending on wave input type. We note that $[H]$ is required only for calculating transmission coefficients in which case only the first column of $[H]^A$ and the first two columns of $[H]$ are needed. Hence, for an efficient implementation, complete matrix-matrix multiplications can be replaced by vector-matrix products for $[H]^A$ (6 elements instead of 36) and half matrix-matrix products for $[H]$ (8 elements instead of 16).

For applications, it is convenient to rearrange terms so that expressions for reflection and transmission coefficients for either an incident P wave or SV wave are obtained from

$$r_p = j_1/j_3, \quad r_s = j_2/j_3, \quad (61)$$

$$t_p = g_1/j_3, \quad t_s = g_2/j_3,$$

where

$$\langle g \rangle = \langle a_0 \rangle [B_1] \cdots [B_n] [a_{n+1}], \quad (62)$$

$$\{j\} = [c_0] [D_1] \cdots [D_n] \{c_{n+1}\},$$

which are built from right to left. The matrices $[a_{n+1}]$, $\{c_{n+1}\}$ are written

$$[a_{n+1}] = \begin{bmatrix} k & \xi \\ -\xi & h \\ 2\mu\xi k & -\gamma \\ -\gamma & -2\mu\xi h \end{bmatrix}_{n+1}, \quad (63)$$

$$\{c_{n+1}\} = \left\{ \begin{array}{l} hk + \xi^2 \\ -\rho s^2 k \\ \xi\gamma - 2\mu\xi hk \\ \xi\gamma - 2\mu\xi hk \\ \rho s^2 h \\ -4\mu^2\xi^2 hk - \gamma^2 \end{array} \right\}_{n+1},$$

while matrices $\langle a_0 \rangle$ and the transpose of $[c_0]$, for a P wave, are given by

$$\langle a_0 \rangle = 2\rho_0 s^2 \langle \gamma/k \quad -2\mu\xi \quad \xi/k \quad -1 \rangle_0, \quad (64)$$

$$[c_0]^T = \begin{bmatrix} 4\mu^2\xi^2 - \gamma^2/hk & 4\mu\xi\gamma/k & 4\mu^2\xi^2 + \gamma^2/hk \\ -\rho s^2/k & 0 & -\rho s^2/k \\ 2\mu\xi + \xi\gamma/hk & 2\gamma/k & 2\mu\xi - \xi\gamma/hk \\ 2\mu\xi + \xi\gamma/hk & -4\mu\xi^2/k & 2\mu\xi - \xi\gamma/hk \\ -\rho s^2/h & 0 & \rho s^2/h \\ -1 + \xi^2/hk & 2\xi/k & -(1 + \xi^2/hk) \end{bmatrix}_0 \quad (65)$$

and for a SV wave by

$$\langle a_0 \rangle = 2\rho_0 s^2 \langle 2\mu\xi \quad \gamma/h \quad -1 \quad -\xi/h \rangle_0, \quad (66)$$

$$[c_0]^T = \begin{bmatrix} -4\mu\xi\gamma/h & 4\mu^2\xi^2 - \gamma^2/hk & 4\mu^2\xi^2 + \gamma^2/hk \\ 0 & \rho s^2/k & -\rho s^2/k \\ 4\mu\xi^2/h & 2\mu\xi + \xi\gamma/hk & 2\mu\xi - \xi\gamma/hk \\ -2\gamma/h & 2\mu\xi + \xi\gamma/hk & 2\mu\xi - \xi\gamma/hk \\ 0 & \rho s^2/h & \rho s^2/h \\ -2\xi/h & -1 + \xi^2/hk & -(1 + \xi^2/hk) \end{bmatrix}_0 \quad (67)$$

Here we could have used a compressed form²³ for $[D_m]$, leading to a fifth-order matrix. However, we found that this brought only slight improvement on computational speed, while making the code more obscure.

Nevertheless, some of the elements of matrices $[B_m]$ and $[D_m]$ exhibit exponential growth with nonzero coefficients. This problem is easily handled through renormalization by multiplying the matrix elements of both $[B_m]$ and $[D_m]$ by $|\exp(-h_m d_m)|$ on each iteration. Finally, the case of normal incidence $\theta_0 = 0^\circ$ is degenerate with respect to both SV waves and SH waves,⁹ and to avoid computa-

tional difficulties, one simply goes to the limit of small values for θ_0 , say of the order of 10^{-2} deg.

To describe the complete time-space response $f(x, z, t)$, one needs to perform a numerical Laplace-Laplace inversion of the transformed solution $\tilde{f}(\xi, z, s)$. A discrete transform pair for Eqs. (6) is made up of a set of sampling points (s_i, ξ_j) in the two-dimensional transformed domain and a set of sampling points (t_i, x_j) in the time-space domain with a functional relationship that connects the two sets. The inverse transform is computed by a Laplace inversion over the ξ_j 's, for each value of s_i , followed by a Laplace inversion over

the s_i 's. A similar procedure is used for the direct transforms needed for the calculation of $\bar{E}_1(\xi, s)$ (beam profile) and $\bar{E}_2(s)$ (pulse shape).

The standard methods²⁴ for the one-sided Laplace transform \mathcal{L}_s , relate a set of samples from $\bar{f}(s)$, taken at equal intervals along the Bromwich contour, to a set of samples from $f(t)$ taken at equally spaced instants in the time domain. Among the various schemes in the literature,²⁴ Durbin's method appears most appropriate for both direct and inverse Laplace transforms. Beskos *et al.*²⁵ improved the method by taking into account that for damped physical systems, both the real and imaginary parts of the transformed solution should behave smoothly at large s_i values. In this case, one may diminish the number of samples in the transformed domain by a factor of 2 or 3 and use an interpolation technique to evaluate $\bar{f}(s)$ as s_i increases. Wilcox and Gibson²⁶ then developed a transform pair whereby the sampling interval is gradually increased with no need for interpolation and no loss of accuracy. In fact, algorithms based on this approach are slower. However, for applications where calculation of $\bar{f}(s_i)$ is by far the more time-consuming operation, use of the Wilcox and Gibson scheme results in significant improvement of computational speed. In our case, each value $\bar{f}(s_i)$ is obtained after many calculations over ξ_j 's, therefore making this transform pair a good choice.

For the two-sided Laplace transform \mathcal{L}_x , we let $\xi = \gamma + i\nu$, so that the direct transform can be written

$$\mathcal{L}_x\{f(x)\} = \int_{-\infty}^{\infty} f(x)e^{\gamma x}e^{i\nu x} dx = \mathcal{F}\{f(x)e^{\gamma x}\} \quad (68)$$

indicating that the calculation may be accomplished by use of a fast Fourier transform (FFT) algorithm. For the inverse transform, one has

$$\mathcal{L}_x^{-1}\{\bar{f}(\xi)\} = \frac{1}{2\pi i} \int_{\gamma - i\infty}^{\gamma + i\infty} \bar{f}(\xi)e^{-\xi x} d\xi, \quad (69)$$

which, after a change of variables, becomes

$$\begin{aligned} \mathcal{L}_x^{-1}\{\bar{f}(\xi)\} &= \frac{e^{-\gamma x}}{2\pi} \int_{-\infty}^{\infty} \bar{f}(\gamma + i\nu)e^{-i\nu x} d\nu \\ &= e^{-\gamma x} \mathcal{F}^{-1}\{\bar{f}(\gamma + i\nu)\}. \end{aligned} \quad (70)$$

Hence, the inverse transform can also be computed by means of a FFT algorithm. Numerical tests indicated that accurate results are obtained for values of the arbitrary parameter γ such that

$$-3 \leq \gamma x_m \leq 0 \quad (71)$$

for x ranging between $-x_m$ to x_m .

Finally, in building our algorithm, we made extensive use of Laplace transform shifting properties, associated with both the time and space variables $t - x$, which provide a high degree of efficiency.

V. NUMERICAL EXAMPLES

First, we consider an example which presented problems in a recent paper by Bogy and Gracewski.⁶ The system

was "water-silver-nickel-copper" (layers 0 to 3, respectively) with material properties given in Table I. The study was conducted for the reflection coefficient $|r_p|$ as a function of the incidence angle θ_0 , for various layer thicknesses. In Fig. 5, we illustrate our results for the energy coefficients R_p , T_p , T_s , where, starting from bottom, the different curves corresponding to $fd_1 = 1.6, 3.2, 4.8, 6.4,$ and 8.0 MHz·mm, respectively; the frequency $f = 4$ MHz and the ratio $d_2/d_1 = 5$ were kept constant. A detailed discussion concerning location of Lamb and Rayleigh poles for different values of d_2/d_1 in the complex ξ plane, may be found in Ref. 6. Again, we mention that taking into account attenuation, causes Rayleigh modes to appear in R_p for angles larger than the shear critical angle.

In the paper by Bogy and Gracewski,⁶ numerical instabilities in $|r_p|$ occurred for $fd_1 > 3.2$ MHz·mm, but the problem would have been even more prominent for transmission. Using the present formulation, the solution is completely stable, therefore allowing study of the resonant mode structure in reflection as well as in transmission for much higher values of fd_1 . We investigated other examples from the literature with equal success. In particular, we were able to extend the results from the recent paper by Cervenka and Chalande⁹ that include fluid layers, to values of fd much higher than 15 MHz·mm, with θ_0 ranging from 0 all the way to 90°.

As a second application, we consider Gaussian beam profiles with sinusoidal temporal excitation. Finite size effects may strongly influence wave propagation, leading to peculiar properties for bounded beams, such as lateral displacement of the reflected component, the so-called Schoch effect, that may occur near the Rayleigh angle.²⁷ In the past, various schemes were put forth that aimed mainly at describing reflection behavior. In cases^{6,28} where the usual Gaussian description, Eq. (11), was used, beamwidth and beam angle effects could be accounted for, but not positioning of source, or focusing. In answer to this, Schmidt and Jensen¹⁰ suggested modeling a bounded beam by an array of equally spaced sources: the position of the array and the number of sources would control beamwidth, while phase differences between sources would command focusing. The drawback here is the large number of adjustable parameters needed to represent realistic Gaussian profiles.

In contrast, our approach, Eqs. (12)–(15), involves only three parameters. In order to evaluate its effectiveness, we examine a simple problem where other models are known to fail. A steel plate of thickness $d = 1.5$ mm and having properties given in Table I, is immersed in water, together with a constant frequency source, $f = 20$ MHz that is located $H_s = 2$ cm above the steel-water interface and produces a Gaussian beam of width $2b = 1$ mm. Similar to the situation depicted in Fig. 4, Lamb modes may be excited when the beam angle is in the range between longitudinal and shear critical angles, $\theta_{cp} < \theta_0 < \theta_{cs}$, while Rayleigh behavior occurs for $\theta_0 = \theta_R \sim 31.2^\circ$. With $\theta_0 = 32^\circ$, Fig. 6 illustrates the behavior of the pressure amplitude in the wave at different altitudes H_0 , above and below the steel-water interface $H_0 = 0$: starting from the bottom, the curves in Fig. 6(a) relate to the incident (negative x values) and reflected (positive x values) beams at observation points $H_0 = 0, 1, 2, 3,$

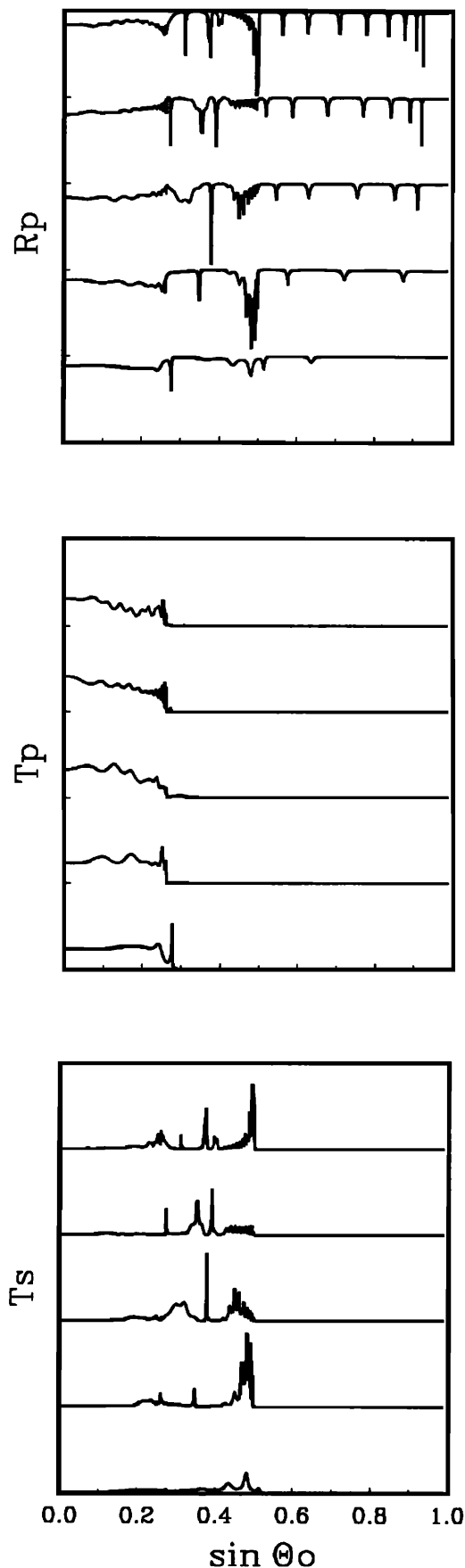


FIG. 5. Angular spectrum of R_p (range 0–1), T_p (range 0–0.5) and T_s (range 0–1) at 4 MHz using Eqs. (55) for the system “water–silver–nickel–copper.” Starting from bottom, $fd_1 = 1.6, 3.2, 4.8, 6.4, 8.0$ MHz·mm and $d_2/d_1 = 5$.

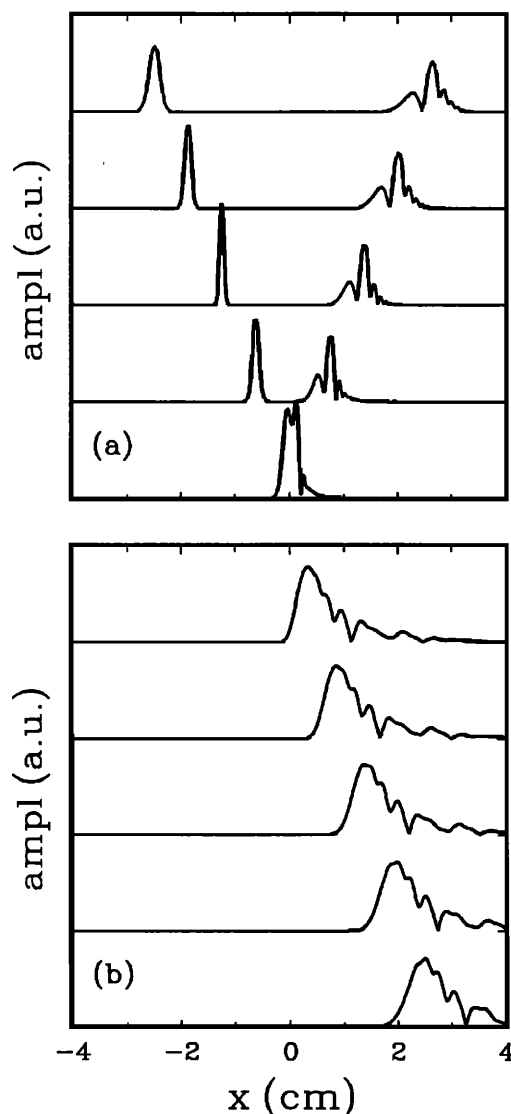


FIG. 6. Acoustic pressure amplitude for the system “water–steel–water;” the source is located $H_s = 2$ cm above the plate and the beam angle is $\theta_0 = 32^\circ$. Different curves correspond to altitudes $H_0 = 0, 1, 2, 3, 4$ cm, (a) above and (b) below the steel plate. The vertical scales in (a) and (b) are in the ratio of 500:1.

and 4 cm, while beginning at the top, the curves of Fig. 6(b) refer to the signal transmitted below the plate at $H_0 = 0, -1, -2, -3, -4$ cm. The pressure amplitudes in Fig. 6 are given in arbitrary units normalized with respect to the maximum value for the reflected signal at the steel–water interface, $H_0 = 0$ in Fig. 6(a); also, the vertical scales in Fig. 6(a) and (b) are in the ratio of 500:1.

As expected, the original beam remains Gaussian-like while progressively diverging as the wave propagates away from the source. At the steel–water interface, the pressure amplitude manifestly departs from a simple Gaussian description, indicative of the complex behavior of the stress/strain fields. Although mainly of specular origin, the reflected beam retains memory of this behaviour, as manifested by the presence of sidelobes and overall complicated shape. The same is also true for the case of the transmitted signal, Fig. 6(b), although its amplitude is very weak.

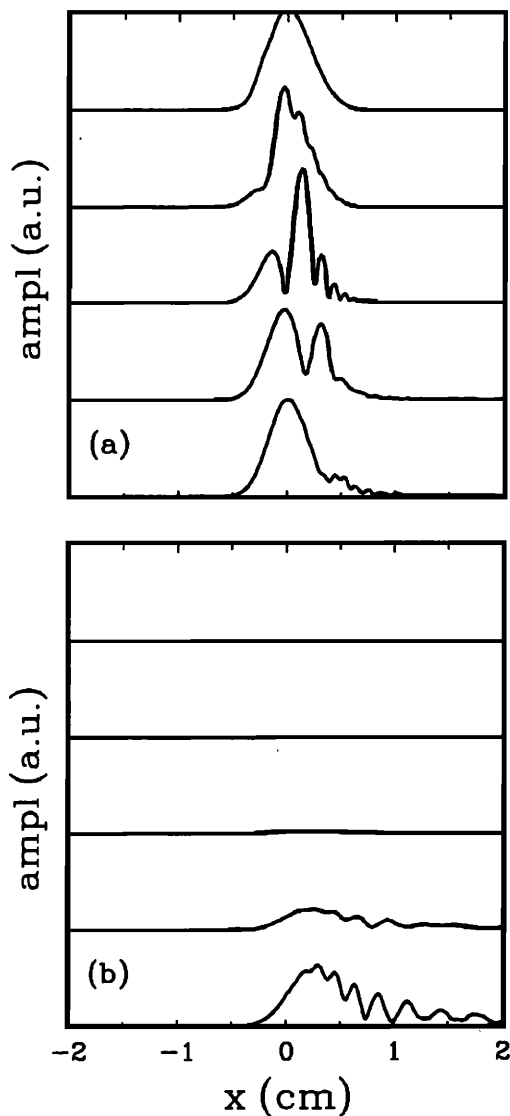


FIG. 7. Acoustic pressure amplitude for the system in Fig. 6 with observation point on the beam axis at $H_0 = 2$ cm, (a) above and (b) below the sample. Starting from bottom, $\theta_0 = 28^\circ, 30^\circ, 32^\circ, 34^\circ, 36^\circ$. The vertical scales in (a) and (b) are in the ratio of 10:1.

In order to gain insight into the description of the acoustic fields, we performed a similar study for different beam angles. The results are illustrated in Fig. 7 where going upwards, the different traces correspond to $\theta_0 = 28^\circ, 30^\circ, 32^\circ, 34^\circ$, and 36° , respectively and observation points located at $H_0 = 2$ cm for the case of Fig. 7(a) and $H_0 = -2$ cm for that of Fig. 7(b). Here, the pressure amplitudes are stated in arbitrary units relative to the maximum value of the reflected signal for $\theta_0 = 28^\circ$ in Fig. 7(a); also, the scales in Fig. 7(a) and (b) are in the ratio of 10:1.

At $\theta_0 = 28^\circ$, one observes oscillations in the transmitted signal, Fig. 7(b), which are suggestive of Lamb modes. Reciprocally, the Lamb modes also influence the reflected signal, Fig. 7(a), but their contribution is quite small compared to specular reflection. As the beam angle increases, the Lamb modes become weaker and disappear almost completely near the Rayleigh angle. This suggests that the pat-

tern in the reflected signal, Figs. 6(a) and 7(a), is associated with Rayleigh behavior: near the Rayleigh angle, $\theta_R \sim 31.2^\circ$, surface waves propagate which leak out energy in the liquid, therefore modulating the amplitude of specular reflection. Here, however, these effects are much more pronounced and they also occur over a much wider range of angles than one would normally anticipate. Clearly, the marked features in Figs. 6 and 7 are also consequent on the specifications for the boundary conditions. In particular, the nulling of the amplitude, which gives the impression for lateral displacement of the beam near $\theta_0 = 32^\circ$ (Schoch effect), are characteristic for the reflection of spherical (cylindrical in our case) waves. In fact, the patterns in Figs. 6(a) and 7(a) would be further complicated in case of a more highly divergent source, due to the additional contribution of the incident wave. Finally, one notes there are no signs of instabilities in the computation of the transmitted signal, even in the presence of evanescent waves when $\theta_0 > 32^\circ$, indicating that our algorithm is very robust.

As a third application, we investigate the time response when the continuous sinusoidal excitation is replaced by a typical experimental pulse. Here, a source having a width $2b = 1$ mm is located at $H_s = 2$ cm above the steel-water interface and generates a pulse of time duration 50 ns and corresponding center frequency 20 MHz. Figure 8(a) relates to normal incidence when the receiver is placed at $H_0 = -2$ cm below the plate, whereas in Fig. 8(b), the angle of incidence is $\theta_0 = 30^\circ$ and the receiver is positioned at $H_0 = 2$ cm above the interface.

Starting from the top of Fig. 8(a), the different traces correspond to the signal that is measured when the receiver is displaced from the center to the right of the propagation axis by $\delta x = 0, 3$, and 6 mm. One observes the different echoes due to reverberation in the plate and also, patterns for $\delta x < 0$ not shown here, would be symmetrical with respect to the propagation axis. For $\delta x = 0$, the time delay between echoes, $\Delta t = 0.52 \mu\text{s}$, and the attenuation correspond exactly to the propagation of longitudinal waves in steel with properties in Table I. On departing from the center line, $\delta x = 0$, beam curvature causes retardation of the echo pattern and the emergence of shear wave echoes ($0.23 \mu\text{s}$ after the longitudinal echoes) through mode conversion. The combined effects of beam curvature and Gaussian distribution of energy lead to the overall decrease in intensity and also to the nonexponential decay of the echo pattern.

In Fig. 8(b), the different traces are obtained, starting from the top, with the receiver displaced from the propagation axis by $\delta x = -6, -3, 0, 3$, and 6 mm. The arrival time for the specularly reflected signal can be calculated simply through

$$\Delta t_0 = \frac{(H_s + H_0)}{c_{p0} \cos \theta_0}, \quad (72)$$

which yields $\Delta t_0 = 31.2 \mu\text{s}$, in good agreement with the numerical results for $\delta x = 0$. Bearing in mind the broadband nature of the acoustic pulse, the results in Fig. 8(b) simply reflect the features for wave interaction described in Fig. 7. Also, with reference to Fig. 6(a), it is clear that the maxi-

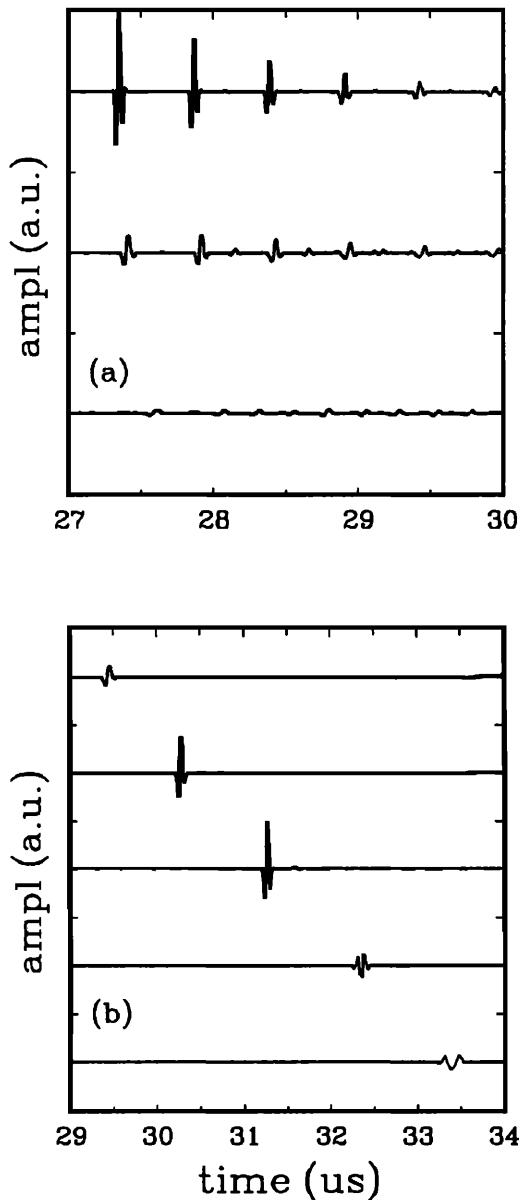


FIG. 8. Pressure wave response of the system in Fig. 7 for deviations from beam axis δx : (a) transmission for $\theta_0 = 0^\circ$ with $\delta x = 0, 3,$ and 6 mm and (b) reflection for $\theta_0 = 30^\circ$ with $\delta x = -6, -3, 0, 3,$ and 6 mm .

imum amplitude is not necessarily at $\delta x = 0$, and that the relationship between time, amplitude and δx is not straightforward. While the signal is weak near $\delta x = 3 \text{ mm}$, it increases at $\delta x = 6 \text{ mm}$ due to the added contribution of leaky Rayleigh waves. This may be confirmed by a simple calculation of the arrival time

$$\Delta t_R = \Delta t_0 + \delta x / c_R, \quad (73)$$

where $c_R = c_{p0} / \sin \theta_R$, leading to $\Delta t_R = 33.3 \mu\text{s}$, in good agreement with the result in Fig. 8(b).

Often, experimental problems are fraught with effects from diffraction that are not exactly tractable. When this occurs, it may be helpful to use transducers with Gaussian beam profiles which help minimize these difficulties. This by no means suppresses the need for close control of experimental conditions, as demonstrated by the results in Figs. 6, 7,

and 8. In this case, however, the details for wave propagation may be interpreted to a high degree of accuracy with the help of a numerical model.

In a final illustration, we examine questions related to viscoelasticity and interfacial properties in view of applications to the characterization of adhesion. For this, we consider a multilayered material that is relevant to industrial uses, such as “steel–polymer (polypropylene)–steel.” Here, we conduct a numerical ultrasonic experiment where the sample and transducer are immersed in water and we compute the frequency dependence for the reflection coefficient of energy R_p in the case of a plane wave at normal incidence. In our example, the thickness, $d_s = 0.4 \text{ mm}$, is the same for both steel plates, while that for the polymer is $d_p = 0.1 \text{ mm}$. The properties for water and steel are those in Table I. On the other hand, we performed ultrasonic measurements on a bulk sample of polypropylene, and found that the results obeyed the relaxation functions in Eqs. (22) with $\rho = 926 \text{ kg/m}^3$, $\lambda_0 = 1.8 \text{ GPa}$, $\lambda_\infty / \lambda_0 = 1.96$, $\mu_0 = 0.0005 \text{ GPa}$, $\mu_\infty / \mu_0 = 4000$. We observed evidence for a wide distribution of relaxation times that changed rapidly, $\tau_p \sim 10^5 \text{ ns}$ to $\tau_p \sim 10^{-2} \text{ ns}$ in the temperature range from 0°C to 150°C , and near $T = 20^\circ \text{C}$, we found $r \sim 1$ and $\tau_p \sim 500 \text{ ns}$.

First, we perform the calculations under the usual assumption of boundary conditions for rigid bonding. The results for R_p (from 0 to 1 between tick marks) in the range from $f = 0$ to $f = 40 \text{ MHz}$ are shown in Fig. 9(a) where, starting from the bottom, the different traces correspond to $\tau_p = 0.1, 1, 10, 100, 10^3,$ and 10^4 ns , respectively. Overall, one sees sharp minimums in R_p located at equally spaced frequencies, $f_{n+1} - f_n = 7.2 \text{ MHz}$, and these coincide with resonant conditions in the steel plate, $f_n = (n/2) c_{ps} / d_s$, $c_{ps} = 5760 \text{ m/s}$ being longitudinal velocity in steel. Also, one notices the occurrence of a low-frequency feature, near $f_0 = 0.5 \text{ MHz}$, which may be interpreted as an eigenmode for the lumped oscillator. In the lower trace, $\tau_p = 0.1 \text{ ns}$, the resonance at $f_1 = 7.2 \text{ MHz}$ corresponds to the limit situation $\omega \tau_p \ll 1$, where the polymer is liquidlike and the attenuation is small. In turn, this condition promotes mode coupling between the different layers, as manifested by the presence of a triple-dip structure near f_1 . As $\omega \tau_p$ approaches 1, the attenuation increases rapidly and the satellite dips become smaller, until eventually only the central feature remains for the resonance of the steel plate. Concurrently, the stiffness in the polymer increases so that the satellites grow deeper and shift slightly to higher frequencies. For $\tau_p = 10 \text{ ns}$ and frequencies above $f_1 = 7.2 \text{ MHz}$, $\omega \tau_p \gg 1$ prevails, so the pattern approaches that of a single steel layer immersed in water, except for the low-frequency feature where $\omega \tau_p \ll 1$. Upon increasing τ_p , the attenuation decreases and the polymer becomes solidlike. In this case, the resonance splitting is even more marked because of the stiffer coupling between the layers.

In our example, the triplet feature for resonance splitting constitutes the most obvious indication of coupling between layers in the sample. Hence, for purposes of nondestructive evaluation, one could test for the presence of this feature through measurements at the appropriate temperature and frequency. However useful, such a test is only spec-

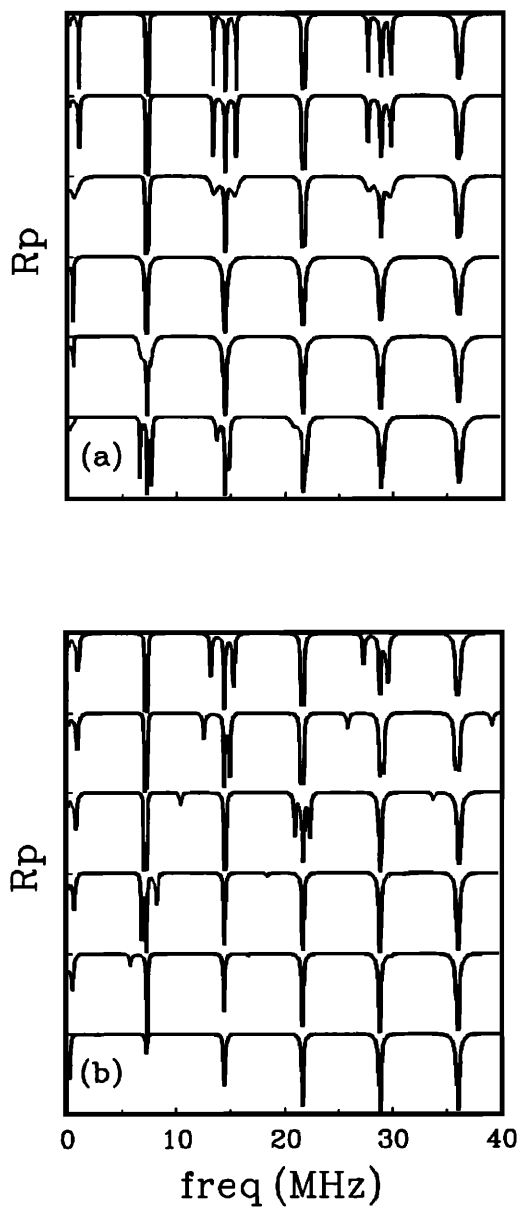


FIG. 9. Frequency spectrum of R_p for a “metal–polymer–metal” sample under water immersion. (a) Rigid bonding and starting from the bottom $\tau_p = 0.1, 1, 10, 100, 10^3, 10^4$ ns. (b) Boundary layer model with $\tau_p = 500$ ns and starting from the bottom $\bar{S}_n = 0.2, 1, 2, 5, 20, 100$.

ulative since the results in Fig. 9(a) presuppose rigid bonding. Actually, this assumption is too stringent and needs to be relaxed. A more realistic model should account for the requirement that the different structures for the metal and the polymer accommodate one another.

As mentioned in Sec. I, the interface between materials may be modeled as an additional viscoelastic layer characterized by its thickness d_i and moduli λ_i and μ_i . We performed a great number of simulations that showed that, whenever d_i was smaller than the acoustic wavelength, the thickness and moduli were not independent parameters. Instead, the data could be scaled over a wide range, which produced a unique description in terms of the normal and transverse specific stiffness coefficients

$$S_n = (\lambda_i + 2\mu_i)/d_i, \quad (74)$$

$$S_t = \mu_i/d_i.$$

This conclusion is in line with a more analytical approach.²¹ Indeed, it turns out that, if the intermediate layer is a small perturbation, the elements of the transfer matrix $[A_i]$ may be written in a form that involves only four parameters: S_n , S_t and the inertia terms m_n and m_p . Then, unless the interface layer is very heavy, m_n and m_p may be safely neglected so that S_n and S_t are the relevant variables in the problem. This is tantamount to the more intuitive idea of an effective viscoelastic spring $S = nk$ where, in a parallel arrangement, n is the number of springs per unit cross section and k the complex spring constant. In reality, accommodation of material properties mostly concerns the polymer, therefore we found it convenient to describe our results in terms of \bar{S}_n and \bar{S}_t normalized with respect to the properties of the bulk polymer

$$\bar{S}_n = S_n d_p / (\lambda_p + 2\mu_p), \quad (75)$$

$$\bar{S}_t = S_t d_p / \mu_p.$$

With $\tau_p = 500$ ns for the bulk polymer at $T = 20$ °C, Fig. 9(b) shows the behaviour of R_p for different values of \bar{S}_n , in the case of normal incidence: starting from the bottom, $\bar{S}_n = 0.2, 1, 2, 5, 20$, and 100. The smallest value, $\bar{S}_n = 0.2$, represents a very weak interface; in fact, the pattern is similar to that for a single steel plate with air backing. For $\bar{S}_n = 1$, there appears a small feature near 5.5 MHz, that shifts to higher frequency for larger values of \bar{S}_n , and eventually contributes to the resonances at $f_1 = 7.2$ MHz ($\bar{S}_n = 2$) and $f_2 = 14.4$ MHz ($\bar{S}_n > 20$). Although this pattern seems to repeat itself with increasing frequency, we found no evidence of a true periodicity. Finally, when $\bar{S}_n > 100$, the behavior approaches that in Fig. 9(a) near $\tau_p = 10^3$ ns, corresponding to rigid bonding.

Compared to the rigid bonding approach, the intermediate layer model leads to a more quantitative and realistic characterization of the forces between the different materials. Indeed, what may be considered as a “good” bond for a specific usage may well turn out to be a “bad” bond for other applications. Therefore, the model provides an interesting tool for the nondestructive evaluation of adhesion.

VI. CONCLUSION

The transfer matrix approach has been improved to provide a complete description for the propagation of ultrasonic waves in multilayered media. Generalized expressions for reflection and transmission coefficients have been derived which were solved numerically. Several computational schemes were examined with respect to numerical stability and a different method was presented that circumvents these difficulties. By transforming and working in the Laplace domain, the scheme was made to handle general relaxation functions for viscoelastic behaviour of solids and liquids alike. The response function for arbitrary beam angles, beam

profiles, and pulse shapes could be obtained through numerical transform inversion. A scenario was suggested for actual implementation on a computer, leading to a very robust and efficient algorithm. Comparative studies based on case examples from the literature served to validate our approach and confirmed its higher degree of reliability. Other examples demonstrated that the scheme provided a complete representation for the frequency, time, and spatial dependence of the acoustic field. Ultimately, boundary conditions for rigid bonding were relaxed and it was shown that adhesion properties between different materials could be modeled through scaling laws.

Because of its robustness, the present scheme is an opportunity for numerous applications. These include planning of experiments for the characterization of materials and design of techniques and strategies for nondestructive testing. Acoustic microscopy could also benefit from accurate modeling, particularly with regard to measurements on biological specimens. Finally, the question of relaxations in confined geometries is a major issue, mainly in relation to adhesion, and this will be the subject of forthcoming papers. In addition, work is ongoing in order to extend the model for applications in anisotropic media.

APPENDIX

Defining the quantities

$$\nu = 2\mu\xi^2/\rho s^2, \quad \eta = \rho s^2/\xi,$$

$$c_h = \cosh(-hd), \quad c_k = \cosh(-kd),$$

$$s_h = \xi/h \sinh(-hd), \quad s_k = \xi/k \sinh(-kd),$$

$$r_h = (h/\xi)^2, \quad r_k = (k/\xi)^2,$$

the matrix $[B_m]$ is given by

$$B_{5-j \ 5-i}^m = B_{ij}^m,$$

$$B_{11} = (1-\nu)c_k + \nu c_h,$$

$$B_{12} = \nu s_k r_k - (1-\nu)s_h,$$

$$B_{13} = (c_k - c_h)/\eta,$$

$$B_{14} = (s_h + s_k r_k)/\eta,$$

$$B_{21} = (1-\nu)s_k - \nu s_h r_h,$$

$$B_{22} = (1-\nu)c_h + \nu c_k,$$

$$B_{23} = (s_k + s_h r_h)/\eta,$$

$$B_{31} = \eta\nu(1-\nu)(c_k - c_h),$$

$$B_{32} = \eta[(1-\nu)^2 s_h + \nu^2 s_k r_k],$$

$$B_{41} = \eta[(1-\nu)^2 s_k + \nu^2 s_h r_h],$$

and for the matrix $[D_m] = [B_m]^\Delta$,

$$D_{7-j \ 7-i}^m = D_{ij}^m,$$

$$D_{11} = c_h c_k + 2\nu(1-\nu)(1-c_h c_k) \\ + [(1-\nu)^2 + \nu^2 r_h r_k] s_h s_k,$$

$$D_{12} = (c_h s_k + c_k s_h r_h)/\eta,$$

$$D_{13} = D_{14} = [(1-2\nu)(1-c_h c_k) \\ - (1-\nu - \nu r_h r_k) s_h s_k]/\eta,$$

$$D_{15} = -(c_h s_k r_k + c_k s_h)/\eta,$$

$$D_{16} = [2(1-c_h c_k) - s_h s_k (1+r_h r_k)]/\eta^2,$$

$$D_{21} = \eta[(1-\nu)^2 c_k s_h + \nu^2 c_h s_k r_k],$$

$$D_{22} = c_h c_k,$$

$$D_{23} = D_{24} = \nu c_h s_k r_k - (1-\nu)c_k s_h,$$

$$D_{25} = -s_h s_k r_k,$$

$$D_{31} = D_{41} = \eta\nu(1-\nu)(1-2\nu)(1-c_h c_k) \\ + \eta[(1-\nu)^3 - \nu^3 r_h r_k] s_h s_k,$$

$$D_{32} = D_{42} = (1-\nu)c_h s_k - \nu c_k s_h r_h,$$

$$D_{34} = D_{43} = D_{33} - 1 = D_{22} - D_{11},$$

$$D_{51} = -\eta(\nu^2 c_k s_h r_h + (1-\nu)^2 c_h s_k),$$

$$D_{52} = -s_h s_k r_h,$$

$$D_{61} = \eta^2 [2\nu^2(1-\nu)^2(1-c_h c_k) \\ - (\nu^4 r_h r_k + (1-\nu)^4) s_h s_k].$$

¹ W. T. Thomson, "Transmission of elastic waves through a stratified solid medium," *J. Appl. Phys.* **21**, 89-93 (1950).

² N. A. Haskell, "The dispersion of surface waves on multilayered media," *Bull. Seism. Soc. Am.* **43**, 17-34 (1953).

³ L. M. Brekhovskikh, *Waves in Layered Media* (Academic, New York, 1960).

⁴ J. W. Dunkin, "Computation of modal solutions in layered, elastic media at high frequencies," *Bull. Seism. Soc. Am.* **55**, 335-358 (1965).

⁵ D. L. Folds and C. D. Loggins, "Transmission and reflection of ultrasonic waves in layered media," *J. Acoust. Soc. Am.* **62**, 1102-1109 (1977).

⁶ D. B. Bogy and S. M. Gracewski, "Nonspecular reflection of bounded acoustic beams from the liquid-solid interface of two elastic layers on a halfspace under water," *Int. J. Solids Struct.* **20**, 747-760 (1984).

⁷ A. H. Nayfeh and T. W. Taylor, "The influence of interfacial conditions on the ultrasonic wave interaction with multilayered media," in *Reviews of Progress in Quantitative* edited by D. O. Thompson and D. E. Chimenti (Plenum, New York, 1988), NDE Vol. 7B.

⁸ T. Kundu and A. K. Mal, "Elastic waves in a multilayered solid due to a dislocation source," *Wave Motion* **7**, 459-471 (1985).

⁹ P. Cervenka and P. Challande, "A new efficient algorithm to compute the exact reflection and transmission factors for plane waves in layered absorbing media (liquids and solids)," *J. Acoust. Soc. Am.* **89**, 1579-1589 (1991).

¹⁰ H. Schmidt and F. B. Jensen, "A full wave solution for propagation in multilayered viscoelastic media with application to Gaussian beam reflection at solid-fluid interfaces," *J. Acoust. Soc. Am.* **77**, 813-825 (1985).

¹¹ N. W. Tschoegl, *The Phenomenological Theory of Linear Viscoelastic Behavior* (Springer-Verlag, Berlin, 1989).

¹² R. E. Challis, T. Alper, R. P. Cocker, A. K. Holmes, and J. D. H. White, "Ultrasonic absorption and velocity dispersion measurements in thin adhesive layers," *Ultrasonics* **29**, 22-28 (1991).

¹³ O. Leroy, G. Quentin, and J. M. Claeys, "Energy conservation for inhomogeneous plane waves," *J. Acoust. Soc. Am.* **84**, 374-378 (1988).

¹⁴ A. N. Norris, "Back reflection of ultrasonic waves from a liquid-solid interface," *J. Acoust. Soc. Am.* **73**, 427-434 (1983).

¹⁵ G. A. Deschamps, "Gaussian beam as a bundle of complex rays," *Electron. Lett.* **7**, 684-685 (1971).

¹⁶ R. M. Christenson, *Theory of Viscoelasticity* (Academic, New York, 1982), 2nd ed.

¹⁷ H. C. Strifors and G. C. Gaunaud, "Selective reflectivity of viscoelastically coated plates in water," *J. Acoust. Soc. Am.* **88**, 901-910 (1990).

¹⁸ R. L. Bagley and P. J. Torvik, "A theoretical basis for the application of fractional calculus to viscoelasticity," *J. Rheol.* **27**, 201-210 (1983).

¹⁹ R. L. Bagley and P. J. Torvik, "On the fractional calculus model of viscoelastic behavior," *J. Rheol.* **30**, 133-155 (1986).

²⁰ K. S. Cole, R. H. Cole, "Dispersion and absorption in dielectrics," *J. Chem. Phys.* **9**, 341-351 (1941).

²¹ S. I. Rokhlin and Y. L. Wang, "Analysis of boundary conditions for elas-

- tic wave interaction with an interface between two solids," *J. Acoust. Soc. Am.* **89**, 503–515 (1991).
- ²² A. K. Mal, C. C. Yin, and Y. Bar-Cohen, "The influence of material dissipation and imperfect bonding on acoustic wave reflection from layered solids," in Ref. 7.
- ²³ F. Schwab and L. Knopoff, "Surface-wave dispersion computation," *Bull. Seism. Soc. Am.* **60**, 321–344 (1970).
- ²⁴ G. V. Narayanan and D. E. Beskos, "Numerical operational methods for time-dependent linear problems," *Int. J. Numer. Methods Eng.* **18**, 1829–1854 (1982).
- ²⁵ D. E. Beskos and A. Y. Michael, "Solution of plane transient elastodynamic problems by finite elements and Laplace transform," *Comp. Struct.* **18**, 695–701 (1984).
- ²⁶ D. J. Wilcox and I. S. Gibson, "Numerical Laplace Transformation and inversion in the analysis of physical systems," *Int. J. Numer. Methods Eng.* **20**, 1507–1519 (1984).
- ²⁷ H. L. Bertoni and T. Tamir, "Unified theory of Rayleigh-angle phenomena for acoustic beams at liquid–solid interfaces," *Appl. Phys.* **2**, 157–172 (1973).
- ²⁸ T. Kundu, A. K. Mal, and R. D. Weglein, "Calculation of the acoustic material signature of a layered solid," *J. Acoust. Soc. Am.* **77**, 353–361 (1985).